Article

Magnetic charge's relaxation propelled electricity in two-dimensional magnetic honeycomb lattice

Magnetic charges on honeycomb vertices

Magnetic charge relaxation between nearest neighbors

Magnetic charge relaxation between next nearest neighbors

Electrical conduction due to magnetic charge relaxation

Yiyao Chen,
George Yumnam,
Jiasen Guo, Laura
Stingaciu, Piotr
Zolnierczuk,
Valeria Lauter,
Deepak K. Singh

singhdk@missouri.edu

HIGHLIGHTS

For the first time, we accurately determine the relaxation time of magnetic charges

We show that magnetic charge mediation propels electrical conduction

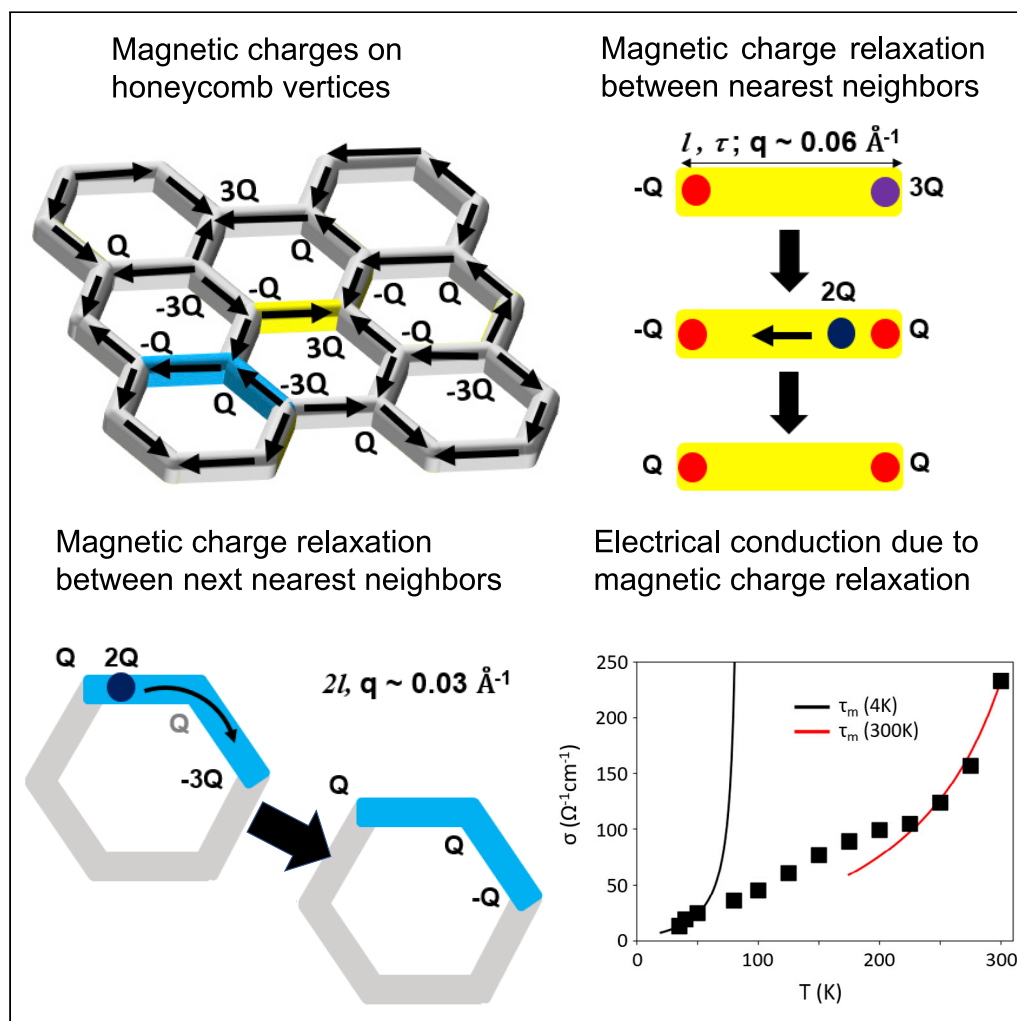We propose a new mechanism for electrical conduction due to magnetic charge relaxation

Article

Magnetic charge's relaxation propelled electricity in two-dimensional magnetic honeycomb lattice

Yiyao Chen,[1] George Yumnam,[1] Jiasen Guo,[1] Laura Stingaciu,[2] Piotr Zolnierczuk,[2,3] Valeria Lauter,[2] and Deepak K. Singh[1,4,*]

SUMMARY

Emerging new concepts, such as magnetic charge dynamics in two-dimensional magnetic material, can provide novel mechanism for spin-based electrical transport at macroscopic length. In artificial spin ice of single domain elements, magnetic charge's relaxation can create an efficient electrical pathway for conduction by generating fluctuations in local magnetic field that couple with conduction electron spins. In a first demonstration, we show that the electrical conductivity is propelled by more than an order of magnitude at room temperature due to magnetic charge defects sub-picosecond relaxation in artificial magnetic honeycomb lattice. The direct evidence to the proposed electrical conduction mechanism in two-dimensional frustrated magnet points to the untapped potential for spintronic applications in this system.

INTRODUCTION

Electrical transport phenomenon is a core physical property of materials. Unlike the well understood metal or semiconductor (Kasap et al., 2017), there are numerous other materials, ranging from magnetic insulator to biological systems, where the underlying mechanism behind electricity propagation is still not understood (Brataas et al., 2012; Hu 2012). For instance, magnon (spin wave) propagation is argued to be the electricity transportation medium in magnetic insulators (Cornelissen et al., 2015). Similarly, proton-based conduction mechanism is proposed to explain electric current flow in biological materials (Ordinario et al., 2014). The unconventional transport mechanism due to the coupling between magnetic moment dynamics and charge's spin is touted to be an efficient electrical transmission process, albeit at low temperature, in solid-state devices (Kajiwara et al., 2010; Zutic et al., 2004). Spin-based conduction, as envisaged in spintronics, is an emergent research arena with immense practical implications (Chappert et al., 2007; Zutic et al., 2004). Recently, an entirely different electrical effect due to magnetic monopole dynamics was proposed in spin ice magnets with peculiar two-in and two-out spin structure on a tetrahedron motif (Bramwell et al., 2009; Bramwell 2012). According to the Dumbbell model's prescription (Castelnovo et al., 2008; Gardner et al., 2010), a magnetic moment is made of magnetic Coulomb's interaction bound two equal and opposite magnetic charges, $\pm Q$ (A.m). In spin ice, the flipping of a moment's direction due to external effect creates a charge defect (monopoles) Q_m of $\pm 2Q$ unit, which traverses the lattice with very little energy loss (Bramwell 2012). Arguably, monopole's dynamics generates non-Maxwellian electricity in applied magnetic field at low temperature, $T < 15$ K, such that $\nabla.B \neq 0$ (Bramwell et al., 2009; Castelnovo et al., 2008; Dunsiger et al., 2011). However, monopole electricity, directly arising due to the monopole's motion, is too weak to be measured directly and is typically inferred from the μSR measurement (Bramwell et al., 2009). Monopole's current need not be confused with conventional electric current. A recent theoretical research has suggested that monopole or magnetic charge defect dynamics causes transverse fluctuation in local magnetic field, which can interact with electric charge carrier (Chern et al., 2013). The indirect interaction between monopole dynamics and electric charge carrier can lead to the efficient electrical conduction process. A necessary condition to realize the magnetic charge dynamic-mediated conduction requires that the charge defect dynamics be confined along a particular direction. Artificial spin ice, such as artificial magnetic honeycomb lattice, with narrow connecting element automatically fulfills this criterion. An outstanding question is: can dynamic charge defect spur an electrical conduction process at high temperature? We have answered this question in the article.

[1]Department of Physics and Astronomy, University of Missouri, Columbia, MO 65211, USA

[2]Neutron Scattering Division, Oak Ridge National Laboratory, Oak Ridge, TN 37831, USA

[3]Forschungszentrum Julich GmbH, JCNS Outstation at SNS, Oak Ridge National Laboratory, Oak Ridge, TN 37831, USA

[4]Lead contact

*Correspondence: singhdk@missouri.edu

https://doi.org/10.1016/j.isci.2021.102206

An artificial spin ice, such as a nanoengineered honeycomb lattice made of single domain magnetic (permalloy, $Ni_{0.81}Fe_{0.19}$) elements (typical length $l \sim 10$ nm), provides a facile platform to explore electrical conduction mediated by magnetic charge defect at higher temperature. The flexibility in tuning constituting element's size, hence the inter-elemental dipolar interaction energy, in an artificial magnetic honeycomb lattice can be exploited to generate magnetic charge defects at high temperature. Previously, magnetic charge defect was shown to mediate electrical conduction in a spin ice material via the interaction between electron's spin, **s**, at the Fermi surface and the transverse local fluctuation in magnetic field **B(k)** due to the monopole dynamics (Chern et al., 2013; Lopez-Bara and Lopez-Aguilar, 2017). According to the formulation, magnetic charge defect's relaxation time plays crucial role in temperature-dependent magnetic charge-mediated conduction, in addition to the residual purely electrical conduction. Following that, a slightly modified equation for conductivity can be written as follows:

$$\sigma = \sigma_0 \left/ \left(1 - A.h \frac{e^{-\Delta/k_B T}}{\varepsilon_F \tau_m}\right) \right. \qquad \text{(Equation 1)}$$

where we use σ_0 as the residual electrical conductivity, given by the Drude's formula $\frac{ne^2\tau_e}{m}$. The dimensionless constant $A\left(\sim \kappa.\frac{k_F}{l_c^{-1}}\right)$ depends on the Fermi wave vector of permalloy, the cutoff length l_c, limited by the thickness of the lattice, for transverse magnetic field fluctuation and a temperature independent constant factor, κ, due to magnetic lattice. Magnetic charge-mediated conductivity also depends on two crucial analytical parameters: Δ and τ_m that represent the threshold energy to create magnetic charge defect and magnetic charge defect's relaxation time, respectively. A key criterion to the applicability of the above formulation (originally envisaged for bulk spin ice materials) requires that the relaxation time, τ_m, in artificial honeycomb lattice be comparable to the spin relaxation time in spin ice magnets. In a honeycomb lattice with two types of magnetic charges, $\pm 3Q$ and $\pm Q$ associated to the all-in or all-out and 2-in and 1-out (or vice versa) magnetic moment correlations (Nisoli et al., 2013; Skjaerrvo et al., 2020), respectively, the threshold energy Δ to create magnetic charge defect $\pm 2Q$ is given by the energy difference $|E_{3Q} - E_Q|$ or $|E_Q - E_{-Q}|$. Here, Q is directly related to magnetic moment M via Q = M/l (Nisoli et al., 2013). Additionally, the unidirectional motion of magnetic charge defect, confined along the length of single domain connecting element due to narrow width and small thickness, can only create transverse fluctuation in local magnetic field, i.e., perpendicular to the direction of motion. While the Fermi surface properties of permalloy (ε_F and k_F) in both the bulk and the thin film are well known (Mijnarends et al., 2002; Petrovykh et al., 1998), the complete lack of information about τ_m forbids any meaningful deduction of electrical conductivity mediated by magnetic charge defect. We have resolved this issue. We precisely determine τ_m using neutron spin echo measurements on a parallel stack of permalloy honeycomb lattice samples. The estimated relaxation time of magnetic charges in permalloy honeycomb, ~ 0.05 ns, is comparable to the $\sim$ picosecond spin relaxation in bulk spin ice (Ehlers et al., 2004), which validates the applicability of Equation (1) to a two-dimensional system. We use the newly acquired knowledge of τ_m to demonstrate the significant enhancement in electrical conductivity due to magnetic charge's relaxation in honeycomb lattice.

RESULTS AND DISCUSSION

Magnetic charge defect relaxation in artificial honeycomb lattice

In a honeycomb lattice, magnetic charges on the vertices undergo transformation by releasing or absorbing charge defect of 2Q unit magnitude (Nisoli et al., 2013; Skjaerrvo et al., 2020). Previously, researchers have used the electron-beam lithography technique to create two-dimensional artificially frustrated structure (Skjaerrvo et al., 2020). However, the large element size of the 2D lattice makes it "athermal" as the inter-elemental dipolar interaction energy, typically of the order of 10^4 K, is much large to achieve in a laboratory (Nisoli et al., 2013; Rougemaille et al., 2011). We overcome this obstacle by utilizing a hierarchical nanofabrication scheme using the diblock template synthesis method, which results in large size honeycomb lattice sample ($\sim$sq. inch) with truly nanoscopic connecting element of permalloy ($Ni_{0.81}Fe_{0.19}$) magnet in the single domain limit ~ 12 nm (length) $\times$ 5 nm (width) $\times$ 8 nm (thickness) (see Supplemental Information) (Chen et al., 2019; Glavic et al., 2018). Consequently, the inter-elemental dipolar energy in the new lattice is very small, ~ 15 K. An important advantage of a small energy scale lies in the feasibility of populating the honeycomb vertices using both $\pm Q$ and $\pm 3Q$ charges at finite temperature. The high integer charges, $\pm 3Q$, are usually accompanied by the high energy cost. Hence, they are not stable. To attend a stable or quasi-stable state of Q or -Q charge, the high integer charges emit or absorb the charge defect of magnitude 2Q unit. The charge defect is highly mobile and traverses the lattice. A
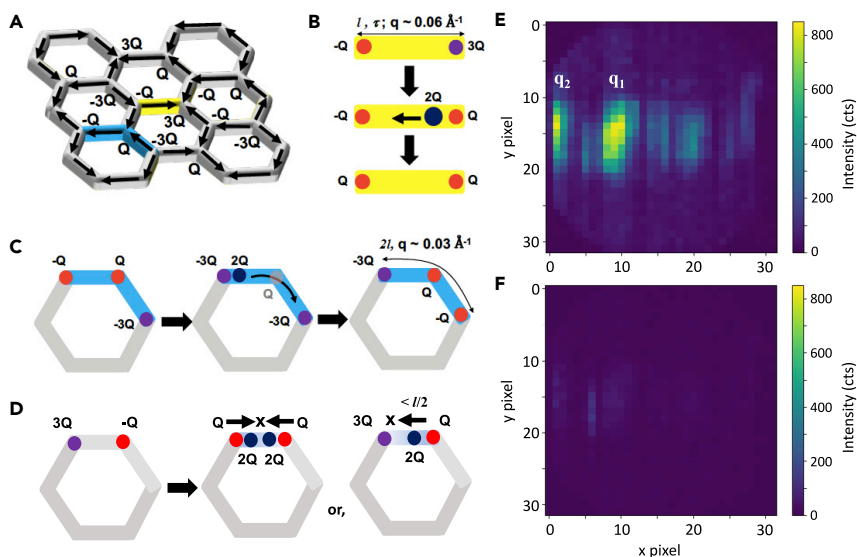
Figure 1. Magnetic charge defect's relaxation in an artificial magnetic honeycomb lattice

(A) Magnetic charges of $\pm Q$ unit and $\pm 3Q$ unit arise due to local magnetic moment arrangements, aligned along the length of connecting element due to shape anisotropy, on the vertices of the honeycomb lattice. At finite temperature, a significant number of vertices in a honeycomb lattice made of single domain size elements (~ 10 nm in length) are occupied by high integer, $\pm 3Q$ unit, charges.

(B–D) High integer charges attend the quasi-stable configuration by releasing or absorbing the magnetic charge defect of $2Q$ unit magnitude. The charge defect relaxes by traversing the length between nearest neighbors (part B) or between the next nearest neighbors (part C). If two charge defects are released in the same direction or a charge defect is released toward a high integer charge of the same polarity, then relaxation is limited to less than half of the length (part D).

(E and F) Experimental evidence to magnetic charge defect's relaxation between nearest and next nearest neighbor vertices via neutron spin echo (NSE) spectroscopy. Each pixel in the color plot corresponds to distinguishable q. Part E shows bright intensities at $q_1 \sim 0.06$ Å^{-1} and $q_2 \sim 0.03$ Å^{-1} (near the y axis) for neutron polarization along $+z$ axis. There is also faint scattering at x-pixel ~ 18, corresponding to the situation D. The absence of bright intensity for neutron polarization along -Z axis (part F) suggests magnetic nature of scattering.

See Figures S1 and S2 for more details of NSE measurement.

schematic description of magnetic charge dynamics in the thermally tunable honeycomb lattice is shown in Figures 1A–1D. The charge defect can travel between the nearest neighbors or between the next nearest neighbors until it faces a high integer charge (3Q or -3Q), which serves as the roadblock. At higher temperature where thermal fluctuation is stronger than $\Delta = |E_Q - E_{-Q}|$ (~ 30 K), the flipping of a magnetic moment associated to the 2-in and 1-out or vice versa configuration can also release a charge defect of $2Q$ unit magnitude. The typical relaxation length of magnetic charge defect corresponds to $q \sim 0.06$ Å^{-1} (between neighboring vertices, Figure 1B) and $q \sim 0.03$ Å^{-1} (between next nearest neighbor vertices, Figure 1C) in reciprocal space.

We indeed observe strong evidences to magnetic charge defect's relaxation at localized q values of ~ 0.06 Å^{-1} and ~ 0.03 Å^{-1} in neutron spin echo (NSE) measurements, see Figure 1E. NSE is a quasi-elastic measurement technique where the relaxation of a magnetic specimen is decoded by measuring relative change in scattered neutron's polarization via the change in the phase current at a given Fourier time (related to neutron precession). The use of NSE technique to elucidate magnetic dynamic properties in magnetic thin film is not common due to weak signal-to-background ratio. To overcome this, we carried out NSE measurements in a modified instrumental configuration at the Spallation Neutron Source (SNS)-NSE spectrometer at the Oak Ridge National Laboratory (ORNL). Here, magnetism in the sample is used as a π flipper to apply $180°$ neutron spin inversion, instead of utilizing a flipper before the sample (Zolnierczuk et al., 2019). Such a modification not only ensures that the detected signal is magnetic in origin but also reduces incident neutron intensity loss. The NSE measurements were performed on a parallel stack of 117 samples of 20×20 mm^2 size to obtain the good signal-to-background ratio. As shown in Figure 1E, the two-dimensional color plot of scattered magnetic intensity for spin-up neutron polarization reveals significant spectral weights at the above mentioned localized q positions. At the same time, little or no
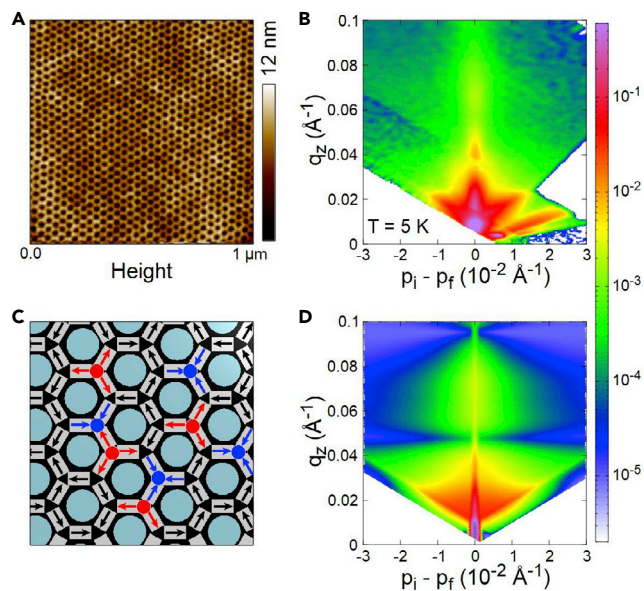
Figure 2. Evidence of finite density of $\pm 3Q$ charges in thermally tunable artificial permalloy honeycomb lattice

(A) Atomic force micrograph of a typical artificial honeycomb lattice.

(B) Off-specular plot, shown as sum of spin-up and spin-down neutrons, of polarized neutron reflectometry (PNR) at T = 5 K (See Figure S5 for specular data of PNR measurement). We follow the typical plotting convention for the off-specular reflectometry graph, i.e., y axis represents the out-of-plane scattering vector ($q_z = \frac{2\pi}{\lambda}(sin\alpha_i + sin\alpha_f)$), and the difference between the z-components of the incident and the outgoing wave vectors ($p_i - p_f = \frac{2\pi}{\lambda}(sin\alpha_i - sin\alpha_f)$) is drawn along the x axis, corresponding to the in-plane correlation (Glavic et al., 2018; Lauter et al., 2016).

(C and D) Numerical modeling of experimental data, as shown in part D, for the magnetic charge configuration, comprising $\pm 3Q$ (red and blue balls) and $\pm Q$ charges on honeycomb vertices, part C, well describes the experimental reflectometry profile in part B.

spectral weight is detected in the spin-down neutron polarization in Figure 1F, confirming the magnetic nature of the signal (also see Figures S1 and S2).

The relaxation of magnetic charge defect is duly affected by the occupation density of energetic $\pm 3Q$ charges. Before determining the relaxation time of charge defects, we quickly show evidence to the occurrence of high integer charges in our honeycomb lattice using polarized neutron reflectometry (PNR) (Lauter et al., 2016). Figure 2A depicts the atomic force micrograph of a typical honeycomb lattice, created using the diblock templating method (see Supplemental Information for detail). PNR measurements were performed on $\sim$ 1 sq. inch size sample in a small guide field of H = 20 Oe to maintain the polarization of incident and scattered neutrons. In Figure 2B, we plot the off-specular intensity measured using spin-up (+) and spin-down (−) neutron at T = 5 K, obtained on MagRef instrument at SNS. The specular reflectivity lies along the x = 0 line in Figure 2B. While the asymmetry between "+" and "-" components in specular data (see Figure S5) infers magnetism in the honeycomb lattice, a broad band of diffuse scattering along the q_x direction suggests in-plane correlation of magnetic charges on honeycomb vertices (Lauter et al., 2016). Experimental data are modeled using the distorted wave Born approximation (DWBA) formulation (see Supplemental Information) to understand the nature of charge correlation (Glavic et al., 2018). As shown in Figure 2D, the numerically simulated reflectometry pattern for magnetic charge configuration, comprising both $\pm Q$ and $\pm 3Q$ charges (shown in Figures 2C), is found to be in good agreement with experimental data. The PNR measurements and the associated DWBA modeling basically suggest that a significant number of honeycomb vertices are indeed occupied by $\pm 3Q$ charges at T = 5 K. At higher temperature, the system is expected to maintain the same or higher density of high integer magnetic charges to generate the sufficient number of relaxing charge defects (Ladak et al., 2010).

Determination of the relaxation time of magnetic charge defects

Next, we quantitatively determine the relaxation time of magnetic charge defect, τ_m, in permalloy honeycomb lattices by analyzing the NSE data at various Fourier times and temperatures. Strong sinusoidal oscillations,
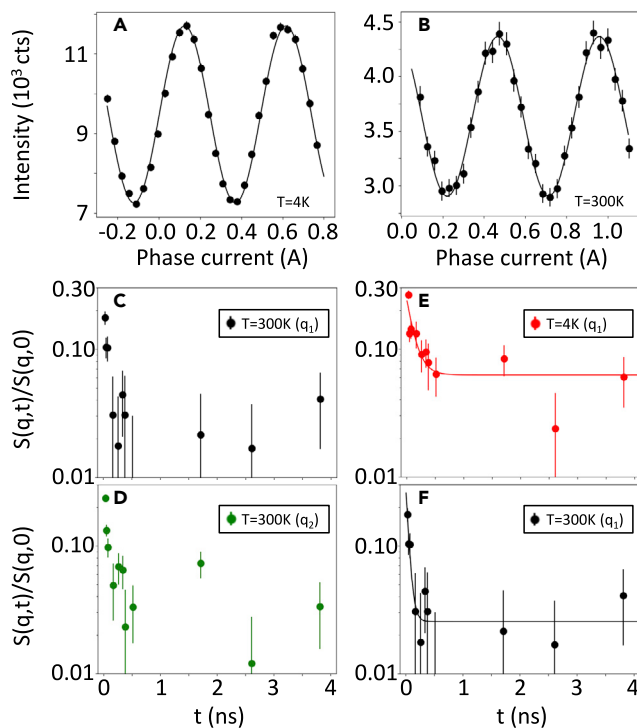
Figure 3. Estimation of magnetic charge defect's relaxation time along honeycomb element

(A and B) Strong signal-to-background ratio is observed in representative spin echo oscillations at T = 4 K (part A) and T = 300 K (part B) at $q_1 \sim 0.06$ Å^{-1} (see Figure S3 for other temperatures).

(C and D) Plot of S(q, t)/S(q, 0) as a function of neutron Fourier time at $q_1 \sim 0.06$ Å^{-1} and $q_2 \sim 0.03$ Å^{-1} at T = 300 K. Sharp slowing down in magnetic relaxation is observed at both q values.

(E and F) Plot of S(q, t)/S(q, 0) as a function of neutron Fourier time at $q_1 \sim 0.06$ Å^{-1} at T = 4 K and T = 300 K. Experimental data are fitted with Equation (2) to extract τ_m at different temperatures. Relaxation is faster at T = 300 K ($\tau_m = 0.049$ ns) than at T = 4 K ($\tau_m = 0.13$ ns), also see Figure S4. Error bars in the plots represent one standard deviation.

reminiscent of high quality spin echo, are observed in NSE measurements at T = 4 K, 15 K, 50 K, and 300 K. Characteristic spin echo plots at T = 4 K and T = 300 K at $q \sim 0.06$ Å^{-1} and at a Fourier time of t = 0.1 ns are shown in Figures 3A and 3B. In Figures 3C and 3D, we show the plots of normalized intensity, S(q, t)/S(q, 0), as a function of the spin echo Fourier time at $q \sim 0.06$ Å^{-1} and 0.03 Å^{-1} at T = 300 K. The normalization is achieved by dividing the observed oscillation amplitude by the maximum measurable amplitude (see Supplemental Information), which is a common practice in magnetic systems with unsettling fluctuation to the lowest measurement temperature (Zolnierczuk et al., 2019). The normalized intensity reduces to the background level above the spin echo's Fourier time of ∼0.5 ns. This is the most general signature of relaxation process in NSE measurements (Ehlers et al., 2006; Zolnierczuk et al., 2019). Fitting of NSE scattering intensity using the typical exponential function yields magnetic charge defect's relaxation time. It is given by (Ehlers et al., 2006) the following equation:

$$\frac{S(q, t)}{S(q, 0)} = C \exp\left(-\frac{t}{\tau_m}\right) \qquad \text{(Equation 2)}$$

where C is constant fitting parameter. While the fluctuation is prominent even at T = 4 K in the honeycomb sample, the slowing down is considerably faster at T = 300 K, see Figures 3E and 3F. The exponential function well describes the relaxation mechanism of magnetic charges. The obtained value of $\tau_m = 0.049$ ns at T = 300 K corresponds to the average magnetic charge defect's velocity of ∼200 m/s. It is at least three times faster than the estimated domain wall velocity in nanostructured magnetic materials (Zhang and Li 2004). At T = 4 K, τ_m increases to 0.13 ns. τ_m at T = 4 K and T = 300 K acts as limits for relaxation at intermediate temperatures.

Electrical conductivity mediated by magnetic charge defects

Finally, we test the hypothesis of electrical conduction mediated by magnetic charge defects in our honeycomb lattice. Although the probability of magnetic charge defect relaxing along the current application direction is
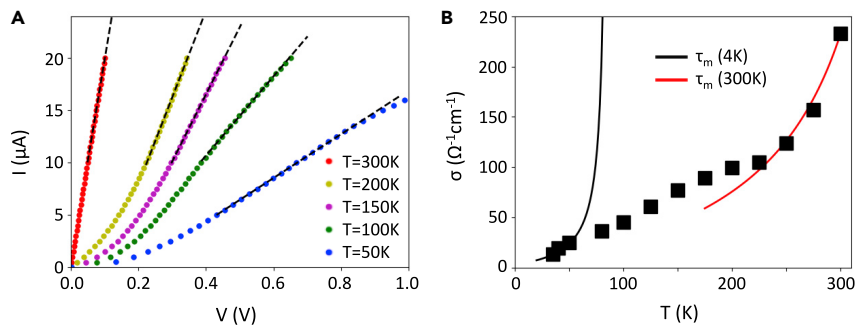
Figure 4. Magnetic charge defect's mediated electrical conductivity in artificial permalloy honeycomb lattice

(A) I-V traces at few characteristic temperatures for permalloy honeycomb (for permalloy thin film see Figure S6). Electrical conductivity is extracted via linear fit to the data.

(B) Plot of conductivity σ vs. temperature. The conductivity increases as temperature increases. We also show theoretically estimated σ due to Equation (1) using τ_m at T = 300 K (red curve) and at T = 4 K (black curve). The value of Δ used to generate the curves, ~ 28 K, is very close to the theoretically estimated value in honeycomb lattice. Temperature-dependent variation in relaxation time forbids a unique fit to the data. Rather, conductivity data lie between the two theoretically generated limiting curves due to relaxation times at T = 300 K and T = 4 K, respectively.

50%, the electrons will drift opposite to the electric field application and interact with magnetic charges in that particular direction. Two conducting processes take place simultaneously: (a) electrons relaxing themselves with finite drift velocity and (b) the drifting electron's spin interacts with the fluctuation in magnetic field due to magnetic charge defect dynamics. Since magnetic charge defect's velocity is significantly higher than electron's drift velocity (typically few μm/s), we can expect to observe a weak background contribution to electrical conductivity due to the mechanism (a). We estimate the dc electrical conductivity of permalloy honeycomb from I-V measurements. Plots of I-V traces at characteristic temperatures are shown in Figure 4A. In Figure 4B, we show the plot of estimated conductivity at different temperatures. There is a noticeable non-linearity in the I-V curve as temperature is reduced below T = 300 K. The small slope at low voltage is most likely associated to the background conductivity due to the purely electric charge carrier's relaxation. As temperature reduces, the background conductivity starts becoming prominent. At low temperature, T < 30 K, the background conductivity becomes comparable to the estimated conductivity due to magnetic charge relaxation.

Since τ_m varies as a function of temperature, unique fit to the conductivity data cannot be obtained. Rather, we generate curves for τ_m at T = 4 K and T = 300 K using Equation (1). For this purpose, we use the standard values of $k_F \sim 1.05$ Å^{-1} and $\varepsilon_F \sim 0.2$ eV for permalloy at low temperature (Mijnarends et al., 2002; Petrovykh et al., 1998). Fermi surface values at higher temperature are corrected using the Fermi-Dirac statistics. The background conductivity due to electron's relaxation, $\sigma_0 \sim 5$ Ω^{-1} cm^{-1}, is kept constant at both temperatures. We see that the conductivity, σ, lies within the two limits imposed by the slower and faster relaxation times at T = 4 K and 300 K, respectively. At room temperature, the conductivity is boosted by more than an order of magnitude with respect to the background conductivity. While the conductivity at higher temperature fits very well to the τ_m (T = 300 K) curve, at lower temperature, the conductivity deviates toward the τ_m (T = 4 K) curve. At intermediate temperature where τ_m (300 K) < τ_m (T) < τ_m (4 K), σ lies between the two limiting curves. It clearly demonstrates the role of new electrical conduction mechanism in 2D honeycomb lattices.

CONCLUSIONS

In summary, we have presented detailed investigation of magnetic charge's relaxation process in two-dimensional artificial permalloy honeycomb lattice. For the first time, the NSE measurement technique is utilized to extract sub-ns relaxation of magnetic charge defect dynamics in an artificial spin ice. More importantly, we have also showed that magnetic charges remain highly dynamic to the lowest measurement temperature in artificial permalloy honeycomb lattice of single domain elements. The ultra-small element size imparts a thermally tunable characteristic to the lattice, which is crucial to the manifestation of magnetic charge-mediated electrical conduction process.

Our comprehensive study reveals a new electrical conduction process in two-dimensional frustrated magnets. Here, we have shown that the electrical conductivity gets a major boost due to magnetic charge's relaxation in a honeycomb lattice. The much stronger conductivity is attributed to charge defect's unidirectional relaxation

(Tomasello et al., 2019), which causes a net drag on the electric charge carrier's drift motion via indirect inter-action with electron's spin. Spin-based electrical conduction at room temperature has been a major challenge, crucial to the development of spintronic system and devices (Zutic et al., 2004). Artificially frustrated geometry can prove a game changer in this quest. Our study also establishes that the modified NSE technique can be utilized to investigate magnetization relaxation properties in a multitude of materials, including magnetic thin film and nanomagnetic devices, which are seemingly difficult at present. Strong understanding of magnetic relaxation in nanodevices (Sun et al., 2005) is highly desirable for technological applications.

Limitations of the study

To understand the role of magnetic charge mediation in electrical conduction in a honeycomb lattice, we have utilized a theoretical formalism that was originally envisaged for the bulk spin ice material. Although the formalism explains the experimental observation of propelled conduction, a more appropriate theoret-ical mechanism for artificial spin ice is needed to better understand the phenomenon. There could also be a new possible mechanism behind the propelled electrical conduction in artificial permalloy honeycomb lat-tices, which we do not know. Our study is limited in that perspective.

Resource availability

Lead contact

Further information and requests for resources and reagents should be directed to and will be fulfilled by the lead contact, Deepak K. Singh (singhdk@missouri.edu).

Material availability

All unique reagents generated in this study are available from the lead contact with a completed Materials Transfer Agreement.

Data and code availability

The published article includes all data sets generated or analyzed during this study.

METHODS

All methods can be found in the accompanying Transparent Methods supplemental file.

SUPPLEMENTAL INFORMATION

Supplemental information can be found online at https://doi.org/10.1016/j.isci.2021.102206.

AUTHOR CONTRIBUTIONS

D.K.S. conceived and supervised every aspect of research. Y.C. and G.Y. made equal contributions to the research. Y.C. and G.Y. made the samples. Y.C., G.Y., J.G., L.S., P.Z., V.L., and D.K.S. performed neutron scattering experiments. Y.C. and G.Y. analyzed and performed numerical modeling of NSE and PNR data. Y.C., G.Y., and J.G. performed electrical measurements. D.K.S. prepared the manuscript with input from all co-authors.

DECLARATION OF INTERESTS

The authors declare no competing interests.

REFERENCES

Bramwell, S.T., Giblin, S.R., Calder, S., Aldus, R., Prabhakaran, D., and Fennell, T. (2009). Measurement of the charge and current of magnetic monopoles in spin ice. Nature *461*, 956–959.

Bramwell, S.T. (2012). Magnetic monopoles: magnetricity near the speed of light. Nat. Phys. *8*, 703–704.

Brataas, A., Kent, A.D., and Ohno, H. (2012). Current-induced torques in magnetic materials. Nat. Mater. *11*, 372–381.

Castelnovo, C., Moessner, R., and Sondhi, S.L. (2008). Magnetic monopoles in spin ice. Nature *451*, 42–45.

Chappert, C., Fert, A., and van Dau, F. (2007). The emergence of spin electronics in data storage. Nat. Mater. *6*, 813–823.

Chen, Y., Summers, B., Dahal, A., Lauter, V., Vignale, G., and Singh, D.K. (2019). Field and current control of the electrical conductivity of an artificial 2D honeycomb lattice. Adv. Mater. *31*, 1808298.

Chern, G.W., Maiti, S., Fernandes, R.M., and Wole, P. (2013). Electronic transport in the Coulomb phase of the pyrochlore spin ice. Phys. Rev. Lett. *110*, 146602.

Cornelissen, L.J., Liu, J., Duine, R.A., Ben Youssef, J., and van Wees, B.J. (2015). Long-distance transport of magnon spin information in a magnetic insulator at room temperature. Nat. Phys. *11*, 1022–1026.

Dunsiger, S., Aczel, A., Arguello, C., Dabkowska, H., Dabkowski, A., Du, M., Goko, T., Javanparast, B., Lin, T., Ning, F., et al. (2011). Spin ice: magnetic excitations without monopole signatures using muon spin rotation. Phys. Rev. Lett. *107*, 207207.

Ehlers, G., Cornelius, A., Fennell, T., Koza, M., Bramwell, S.T., and Gardner, J.S. (2004). Evidence for two distinct spin relaxation mechanisms in 'hot' spin ice $Ho_2Ti_2O_7$. J. Phys. Condens. Matter *16*, S635.

Ehlers, G., Gardner, J.S., Booth, C.H., Daniel, M., Kam, K.C., Cheetham, A.K., Antonio, D., Brooks, H.E., Cornelius, A.L., Bramwell, S.T., et al. (2006). Dynamics of diluted Ho spin ice $Ho_{2-x}Y_xTi_2O_7$ studied by neutron spin echo spectroscopy and ac susceptibility. Phys. Rev. B *73*, 174429.

Gardner, J.S., Gingras, M.J.P., and Greedan, J.E. (2010). Magnetic pyrochlore oxides. Rev. Mod. Phys. *82*, 53.

Glavic, A., Summers, B., Dahal, A., Kline, J., van Herck, W., Sukhov, A., Ernst, A., and Singh, D.K. (2018). Spin solid versus magnetic charge ordered state in artificial honeycomb lattice of connected elements. Adv. Sci. *5*, 1700856.

Hu, X. (2012). Half-metallic antiferromagnet as a prospective material for spintronics. Adv. Mater. *24*, 294–298.

Kajiwara, Y., Harii, K., Takahashi, S., Ohe, J., Uchida, K., Mizuguchi, M., Umezawa, H., Kawai, H., Ando, K., Takanashi, K., et al. (2010). Transmission of electrical signals by spin-wave interconversion in a magnetic insulator. Nature *464*, 262–266.

Kasap, S., Koughia, C., and Ruda, H.E. (2017). Electrical conduction in metals and semiconductors. In Handbook of Electronic and Photonic Materials, S. Kasap and P. Capper, eds. (Springer Publication)), pp. 19–45, Chap. 2.

Ladak, S., Read, D., Perkins, G., Cohen, L., and Branford, W. (2010). Direct observation of magnetic monopole defects in an artificial spin-ice system. Nat. Phys. *6*, 359.

Lauter, V., Lauter, H., Glavic, A., and Toperverg, B. (2016). Reference Module in Materials Science and Materials Engineering (Elsevier), pp. 1–27.

Lopez-Bara, F.I., and Lopez-Aguilar, F. (2017). Analysis of electromagnetic propagation in the magnetic plasma state in spin-ice systems. J. Appl. Phys. *121*, 175108.

Mijnarends, P.E., Sahrakorpi, S., Lindroos, M., and Bansil, A. (2002). Angle-resolved photoemission spectra, electronic structure, and spin-dependent scattering in $Ni_{1-x}Fe_x$ Permalloys. Phys. Rev. B *65*, 075106.

Nisoli, C., Moessner, R., and Schiffer, P. (2013). Colloquium: artificial spin ice: designing and imaging magnetic frustration. Rev. Mod. Phys. *85*, 1473.

Ordinario, D.D., Phan, L., Walkup, W.G., Jocson, J.-M., Karshalev, E., Husken, N., and Gorodetsky, A.A. (2014). Bulk protonic conductivity in a cephalopod structural protein. Nat. Chem. *6*, 596–602.

Petrovykh, D.Y., Altmann, K.N., Hochst, H., Laubscher, M., Maat, S., Mankey, G.J., and Himpsel, F.J. (1998). Spin-dependent band structure, Fermi surface, and carrier lifetime of permalloy. Appl. Phys. Lett. *73*, 3459.

Rougemaille, N., Montaigne, F., Canals, B., Duluard, A., Lacour, D., Hehn, M., Belkhou, R., Fruchart, O., Moussaoui, S., Bendounan, A., and Maccherozzi, F. (2011). Artificial kagome arrays of nanomagnets: a frozen dipolar spin ice. Phys. Rev. Lett. *106*, 057209.

Skjaerrvo, S.H., Marrows, C.H., Stamps, R.L., and Heyderman, L.J. (2020). Advances in artificial spin ice. Nat. Rev. Phys. *2*, 13–28.

Sun, L., Hao, Y., Chien, C.-L., and Searson, P.C. (2005). Tuning the properties of magnetic nanowires. IBM J. Res. Dev. *49*, 79.

Tomasello, B., Castelnovo, C., Moessner, R., and Quintanilla, J. (2019). Correlated quantum tunneling of monopoles in spin ice. Phys. Rev. Lett. *123*, 067204.

Zhang, S., and Li, Z. (2004). Roles of nonequilibrium conduction electrons on the magnetization dynamics of ferromagnets. Phys. Rev. Lett. *93*, 127204.

Zolnierczuk, P.A., Holderer, O., Pasini, S., Kozielewski, T., Stingaciu, L.R., and Monkenbusch, M. (2019). Efficient data extraction from neutron time-of-flight spin-echo raw data. J. Appl. Cryst. *52*, 1022–1034.

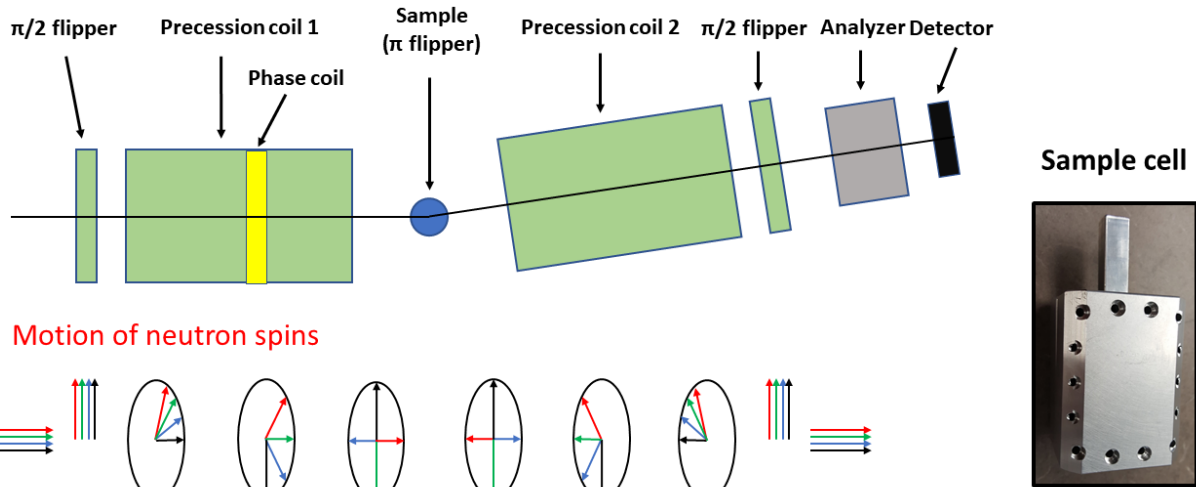Zutic, I., Fabian, J., and Sarma, S.D. (2004). Spintronics: fundamentals and applications. Rev. Mod. Phys. *76*, 323.

Supplemental information

Magnetic charge's relaxation propelled

electricity in two-dimensional

magnetic honeycomb lattice

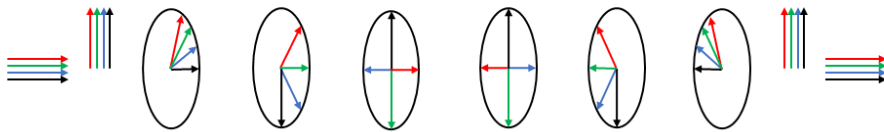Yiyao Chen, George Yumnam, Jiasen Guo, Laura Stingaciu, Piotr Zolnierczuk, Valeria Lauter, and Deepak K. Singh

Figure S1. Schematic of the NSE spectrometer and motion of neutron spins. Related to Figure 1.
The first π/2 flipper starts the neutron precession by flipping the horizontal polarization perpendicular to the magnetic field generated from the first precession coil. Neutrons with different wavelength (and velocity) experience different pression phases and start to depolarize. A π flipper reverses the precession plane and the second precession coil reverses the precession phase accumulation from the first precession coil. The second π/2 flipper stops the precession and turns the recovered polarization in the direction of the analyzer. The schematics shows a fully recovered polarization for elastic scattering on an ideal instrument. For quasi-elastic measurements the polarization will not be completely recovered. The inset shows a picture of the custom-made sample cell, which has the capacity of 44 mm sample thickness.
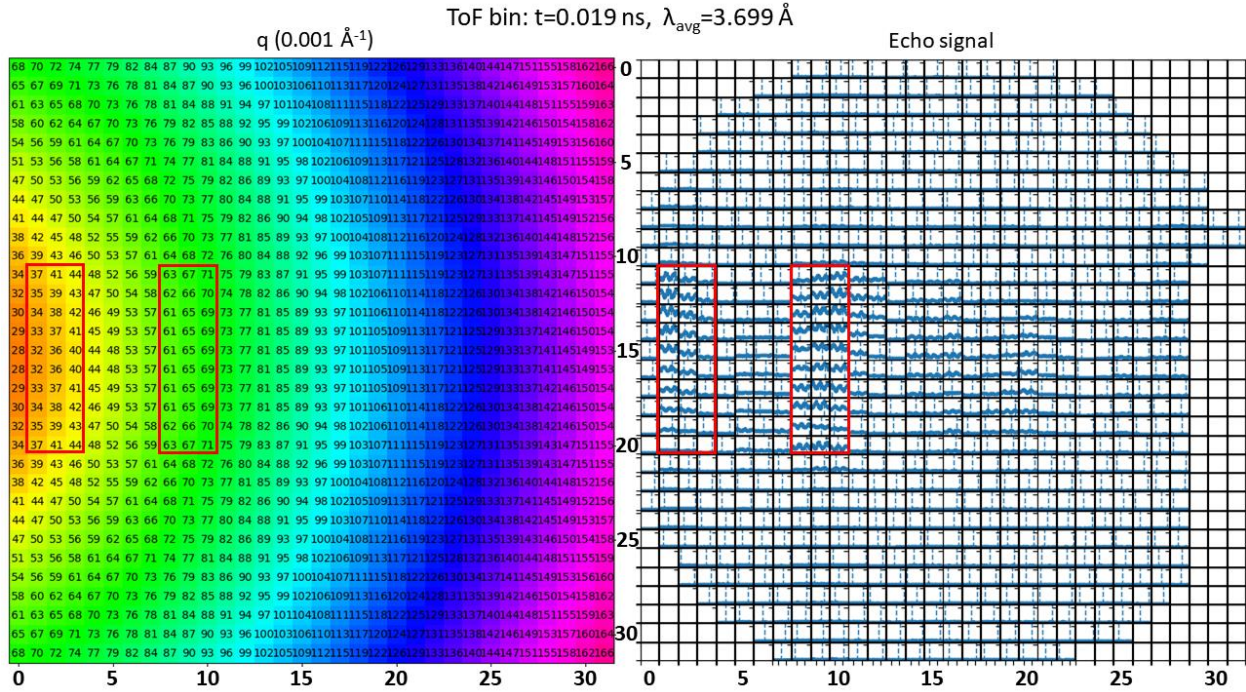
Figure S2. Q rings and echo signals on NSE detector. Related to Figure 1. Left panel shows the calculated q values (in units of 0.001 Å^{-1}) on each detector pixel for t = 0.1 ns measurement ToF bin 4. Right panel shows the echo signals in each detector pixel for T=4 K, t = 0.1 ns measurement ToF bin 4. The x and y axis are detector pixel numbers along the x and y direction. Clear echo signals are observed in specific q regions.
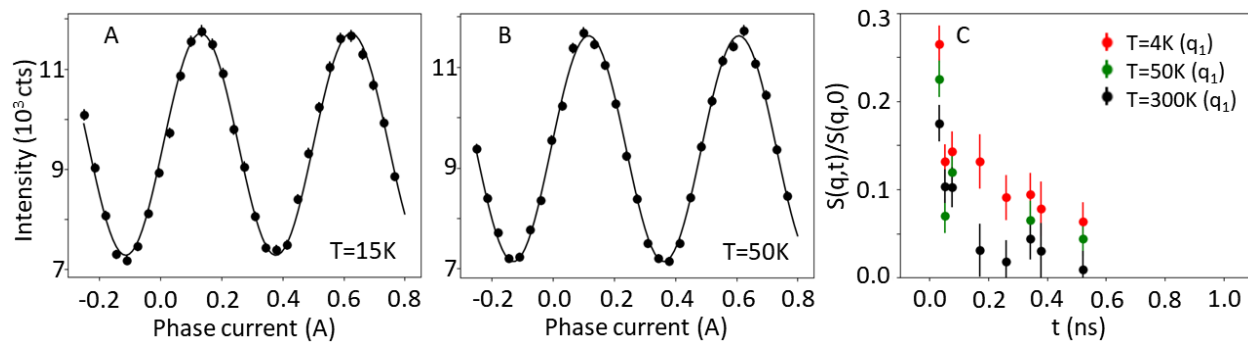
Figure S3. Echo intensities and intermediate scattering function from NSE measurement. Related to Figure 3. (A-B) Spin echo oscillations at T = 15 K and T =50 K at $q_1 \sim 0.06$ Å^{-1}. (C) Calculated intermediate scattering function $S(q,t)/S(q,0)$ at q_1 range.
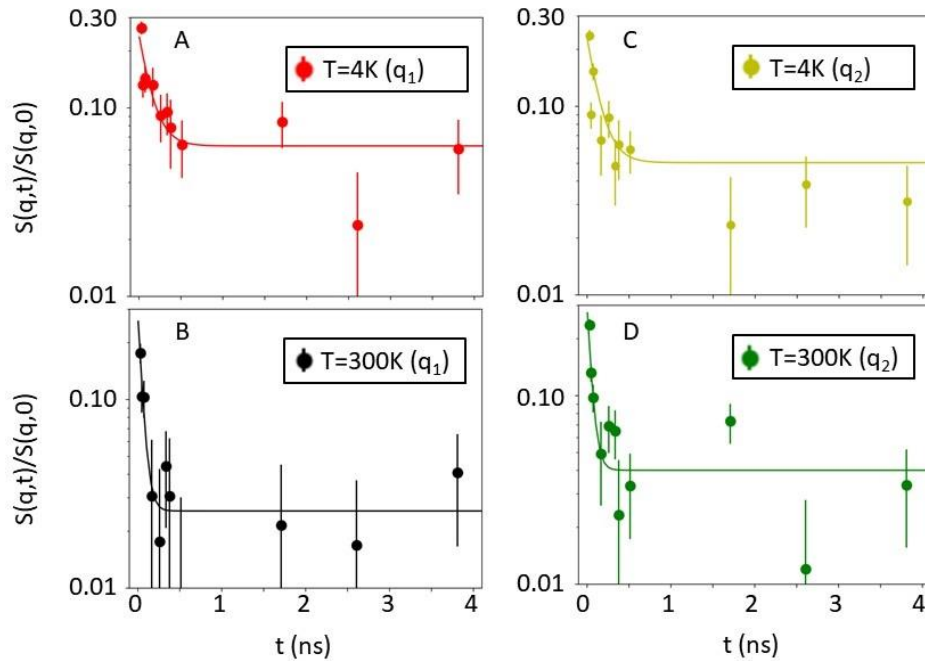
Figure S4. Magnetic charge defect's relaxation at different q ranges. Related to Figure 3. (A-B) Intermediate scattering function $S(q, t)/S(q, 0)$ at $q_1 \sim 0.06$ Å^{-1} range, experimental data is fitted to extract τ_m, replotted from Figure 3E-F. (C-D) Intermediate scattering function $S(q, t)/S(q, 0)$ at $q_2 \sim 0.03$ Å^{-1} range, the solid line is plotted with the same τ_m parameter from q_1 range (τ_m=0.049 ns for T = 300 K and τ_m = 0.13 ns for T = 4 K) and describes the data well. τ_m at q_1 and q_2 are comparable at both temperatures.

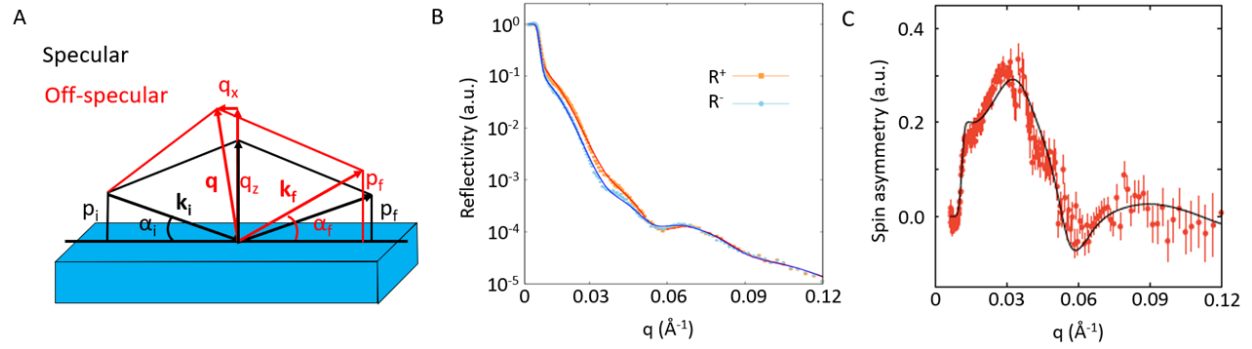**Figure S5. Schematic and specular reflectivity result of PNR measurement. Related to Figure 2.** (A) Schematic of PNR measurement. (B) Measured and fitted spin resolved specular reflectivity for neutrons with spin-up (R^+) and spin-down (R^-). A clear separation between the spin-up and spin-down reflectivities is observed. (C) Measured and fitted spin asymmetry $(R^+ - R^-)/(R^+ + R^-)$ as a function of q.
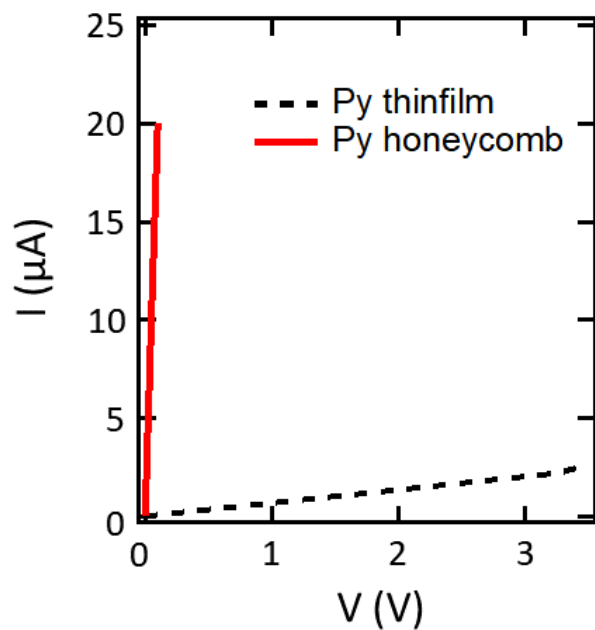
Figure S6. I-V characteristic from permalloy thin film at T = 300 K. Related to Figure 4. The permalloy thin film and permalloy honeycomb lattice have comparable thickness. The conductivity of thin film is much smaller than the honeycomb lattice.

Transparent Methods

Nanofabrication method of artificial permalloy honeycomb lattice.
Fabrication of artificial magnetic honeycomb lattice starts with the synthesis of porous hexagonal diblock template on top of a silicon substrate. The template fabrication process utilizes diblock copolymer polystyrene(PS)-b-poly-4-vinyl pyridine (P4VP) of molecular weight 29k Dalton with the volume fraction of 70% PS and 30% P4VP. The diblock copolymer tends to self-assemble, under right condition, in a hexagonal cylindrical structure of P4VP in the matrix of polystyrene. A 0.5% PS-b-P4VP copolymer solution in toluene was spin coated onto cleaned silicon wafers at 2500 rpm for 30 s. After spin coating, the samples were solvent annealed at 25 °C for 12 hours in a mixture of THF/toluene (80:20 v/v) environment. The process results in the self-assembly of P4VP cylinders in a hexagonal pattern within a PS matrix. Submerging the samples in ethanol for 20 minutes releases the P4VP cylinders yielding a porous hexagonal template. Reactive ion etching with CF_4 gas was performed to transfer the hexagonal pattern to the underlying silicon substrate. The top layer of the substrate resembles a honeycomb lattice pattern. This topographical property is exploited to create magnetic honeycomb lattice by depositing permalloy, $Ni_{0.81}Fe_{0.19}$, on top of the uniformly rotating substrate in near parallel configuration (~1°) in an electron-beam evaporation. This allowed evaporated material to coat the top surface of the honeycomb only, producing the desired magnetic honeycomb lattice with a typical element size of 12 nm (length) × 5 nm (width) × ~8 nm (thickness).

Neutron spin echo instrument configuration detail.
The neutron spin echo (NSE) measurements were performed on an ultrahigh resolution (2 neV) neutron spectrometer SNS-NSE at beam line BL-15 of Spallation Neutron Source, Oak Ridge National Laboratory (Ohl et al., 2012). The instrument utilizes the time of flight technique and was operated with a neutron wavelength span of 3.5 Å to 6.5 Å (3 Å bandwidth) for the experiment. The neutron beam was measured with a 30 cm × 30 cm 2D position sensitive ^{3}He detector at 3.9 m from the sample. Since the magnetic sample itself does a π flip of the neutron (spin inversion), the instrument was modified from the standard operation setup. The π flipper before the sample position was removed and extra magnetic coils were installed for three-directional neutron polarization analysis. To obtain good signal-to-background ratio, 117 samples of ~20×20 mm^2 surface area were stacked together and loaded in the custom-made sample cell (shown in Figure S1). The sample cell was inserted into the close cycle refrigerator with a base temperature of T = 4 K.

NSE experiment investigates the dynamical processes of the sample. The Fourier time t is defined as,

$$t = \frac{\gamma}{2\pi}\left(\frac{m}{h}\right)^2 J\lambda^3, \tag{1}$$

where γ is neutron gyromagnetic ratio, m is the neutron mass, h is Planck's constant, and $J = \int |B|\,dl$ is the magnetic field integral along the neutron path (Zolnierczuk et al., 2019). At a fixed wavelength λ, the Fourier time is controlled by the choice of field integral J from the precession coils. The field integral J from precession coil 1 and precession coil 2 are the same, so that the second coil reverses the spin precession phase manipulation from the first coil. A phase current (converts to dJ with an instrumental coefficient) runs through the phase coil to provide an extra precession phase before the neutron reaches the analyzer.

Analysis of neutron spin echo data.
The echo signal manifests the NSE measurement of the recovered neutron polarization as a function of neutron precession phase current. The echo intensity from a single wavelength λ simply follows a cosine function,

$$I(\phi) = A\cos(\phi\lambda) + B, \tag{2}$$

where the phase $\phi = (dJ - dJ_0)\gamma\frac{m}{h}$ is directly related with the phase current (dJ). If neutron has a wavelength span of $\lambda_{avg} \pm d\lambda$, the signals from all different wavelengths add up. The total intensity follows the following relation,

$$I(\phi) = A\cos\left(\phi\lambda_{avg}\right)\frac{\sin(\phi d\lambda)}{\phi d\lambda} + B. \tag{3}$$

Here it is assumed that all wavelengths in the bandwidth of $2d\lambda$ have the same flux. After including a neutron flux weighted summation (instead of the uniformly weighted summation), it is exactly the same as Eq. 7 from Zolnierczuk et al., (2019). We note that the decay type feature of the cosine amplitude comes from the term $\sin(\phi d\lambda)/(\phi d\lambda)$. If $d\lambda$ is very small, the term becomes 1 and the amplitude decay is negligible.

NSE raw data treatment.
Neutron spin echo measurements were performed with neutron wavelength range of 3.5 Å to 6.5 Å. Experimental data was binned into 42 different time of flight (ToF) wavelength channels, with λ_{max}~3.5 Å in ToF bin 0 and λ_{max}~6.5 Å in ToF bin 41. (Fourier time t = 0.1 ns measurement refers to t ~ 0.1 ns in ToF bin 41 and t ~ 0.015 ns in ToF bin 0). The position sensitive detector has 32 channels along the x-direction and 32 channels along the y-direction. As a result, NSE data point forms 42 ToF bins of 32 x pixels × 32 y pixels array (see Figure S2). All individual pixel counts are first normalized by the proton charge (PC) value during its specific phase current measurement followed by a multiplication by the average PC value during the whole scan.

The echo signals are not always in phase between different pixels and ToF bins. Even signals in adjacent pixels can be completely out of phase as shown in Figure S2. Correction for the phase shift needs to be done before summing up the neutron counts in the individual detector pixels from different ToF bins.

In the end, we obtained echo intensities by adding up the pixels along x, y directions on the detector then summing over different ToF bins, while taking care of phase correction before the summation process. The echo intensities plotted in Figure 3A (T = 4 K) and Figure 3B (T = 300 K) summed over the range of x = 8 to 10, y = 11 to 20 in ToF bin = 4. The echo intensities at T=15 K and 50 K are shown in Figure S3A-B. The intermediate scattering function plots in Figure 3C and Figure 3D summed over more ToF bins. q_1 was summed over the range of x=8 to 10, y=10 to 21. q_2 was summed over the range of x = 1 to 3, y = 10 to 21. ToF bin = 10 to 19, 20 to 29, and 30 to 39 were explored.

NSE intermediate scattering function calculation.
The end goal of the NSE data analysis is to get the intermediate scattering function S(q,t)/S(q,0). After fitting the echo intensities to get the echo amplitude A, the intermediate scattering function can be calculated from dividing the measured echo amplitude by the maximum measurable amplitude.
For non-magnetic samples,

$$\frac{S(q,t)}{S(q,0)} = \frac{2A}{U-D} \tag{4}$$

where U and D are the spin-up (non spin flip) and spin-down (spin flip) intensities. For magnetic samples, half of the magnetic intensity M/2 is used as the normalization factor instead of (U-D) (Pappas et al., 2006). Three-directional neutron polarization analysis (also referred to as xyz polarization analysis) measures six cross sections with the magnetic field along three axes x, y, and z, up and down for each axis. The magnetic intensity is calculated from xyz polarization measurements by using

$$M = 2\left(z_{up} - z_{dn}\right) - \left[\left(x_{up} - x_{dn}\right) + \left(y_{up} - y_{dn}\right)\right]. \tag{5}$$

Comparing with

$$U = (x_{up} + y_{up} + z_{up})/3, \ \ D = (x_{dn} + y_{dn} + z_{dn})/3, \tag{6}$$

M/2 << (U-D). The intermediate scattering function for magnetic samples is calculated from

$$\frac{S(q,t)}{S(q,0)} = \frac{2A}{M/2} = \frac{4A}{M}. \tag{7}$$

In our NSE data analysis, the results of 4A/M were comparable with 30A/(U-D). For each chosen range of x pixel, y pixel and ToF bin of the echo signal, the normalization factor was calculated separately from the xyz polarization measurements with the exact same x pixel, y pixel and ToF bin range.

The dynamic structure factor S(q, ω) is convoluted with the instrumental resolution R(q, ω), what we get from the experiment is S_{exp}(q, ω)=S(q, ω)* R(q, ω). The intermediate scattering function is the Fourier transform of the dynamic structure factor, $S(q,t) = \int S(q,\omega) \cos(\omega t)\, d\omega$. Thus the instrumental resolution can be simply divided out from S_{exp}(q, t)=S(q, t)R(q, t), and 0<R(q, t)<1.(*1*) In our case the relaxation of magnetic charge is still significant at T = 4 K, dividing the high temperature data by T = 4 K data for instrumental resolution correction is not sufficient. Also, the error bars are too big in such normalization. The conclusion of a smaller relaxation time at higher temperature for our magnetic sample is still solid without the instrumental resolution correction, because the correction would only shift the values of relaxation time at different T towards the same direction. Plot of S(q, t)/ S(q, 0) at various temperatures of T = 4 K, 50 K and 300 K are shown in Figure S3C. The relaxation of magnetic charges at T = 4 K to T = 50 K are found to be qualitatively similar.

Every data point in the intermediate scattering function S(q,t)/S(q,0) (Figure S3C) is extracted from the fitting of the treated raw data (Figure S3A-B). Statistics of the raw data is essential to extract a reliable τ_m from fitting of the intermediate scattering function. Two q ranges of NSE data (q_1 ~ 0.06 Å^{-1} and q_2 ~ 0.03 Å^{-1}) were explored in the data analysis, we used q_1 range to extract the magnetic relaxation time τ_m. Data from q_2 range have less statistics compared with q_1 range because q_2 range was too close to the detector edge (no data on x=0 pixel). We plotted the exponential function with τ_m extracted from q_1 range and it also describes data from q_2 range quite well, see Figure S4C-D.

Polarized neutron reflectometry (PNR) measurements and distorted wave Born approximation (DWBA) simulation details.
Polarized neutron reflectometry (PNR) measurements were performed on a 20×20 mm^2 surface area sample at the Magnetism Reflectometer, beam line BL-4A of the Spallation Neutron Source (SNS), at Oak Ridge National Laboratory (ORNL), see Figure S5A for a schematic of PNR measurement. The instrument utilizes the time of flight technique in a horizontal scattering geometry with a bandwidth of 5.6 Å (wavelength varying between 2.6 - 8.2 Å). The beam was collimated using a set of slits before the sample and measured with a 2D position sensitive ^{3}He detector with 1.5 mm resolution at 2.5 m from the sample. The sample was mounted on the copper cold finger of a close cycle refrigerator with a base temperature of T=5 K. Beam polarization and polarization analysis was performed using reflective super-mirror devices, achieving better than 98% polarization efficiency over the full wavelength band. For reflectivity and off-specular scattering the full vertical divergence was used for maximum intensity and a 5% Δθ/θ≈Δq$_z$/q$_z$ relative resolution in horizontal direction. A small guide field of H = 20 Oe was applied in-plane to the sample to maintain polarization of incident and scattered neutrons for the experiment. Figure S5B shows the specular reflectivity at T=5 K from the PNR measurement shown in Figure 2B. The specular reflectivity clearly shows the separation of spin-up (R$^+$) and spin-down (R$^-$) reflectivities, hence indicating the presence of net magnetic moment in the system. Estimated magnetization, obtained from the fitting of spin asymmetry (SA), defined as (R$^+$ - R$^-$)/(R$^+$ + R$^-$), plot as a function of wave-vector, yields a magnetic moment of 0.78(2) A/m in magnetic honeycomb lattice, see Figure S5C.

The Off-Specular reflectivity profiles were simulated based on the Distorted-Wave Born-Approximation (DWBA) as implemented in the BornAgain software (Burle et al., 2018). The lattice models used in these simulations follows our prior work (Glavic et al., 2018). The model of our simulation is based on the nuclear and magnetic scattering length density profiles obtained from the fitted specular neutron reflectivity data at 5 K (as shown in Figure S5B), fitted using Licorne-Py software (Lauter et al., 2019). For the DWBA off-specular simulation, the sample is constructed as a multilayer consisting of a substrate layer along with 3 layers (*l*) on top, for which the scattering matrix elements can be expressed by:

$$\langle \psi_i | \delta v | \psi_f \rangle = \sum_l \sum_{\pm i} \sum_{\pm f} \langle \psi_{il}^{\pm} | \delta v | \psi_{fl}^{\pm} \rangle, \tag{8}$$

where, v is the first order perturbation expansion term of scattering length density v($\mathbf{r}$), and ψ_i, ψ_f denotes the incident, and final wavefunctions, respectively. The forward or backward traveling wavefunction in real-space is given by ψ^+ and ψ^- respectively. The bottom-layer is composed of nanostructured silicon with honeycomb patterns, and the next layer, permalloy-layer, comprises of nanostructured permalloy with incoherent magnetic phase. The top-layer is made of a thin layer of partially oxidized permalloy. An ambient air layer was placed on top of the oxidized permalloy-layer. We introduced a layout of honeycomb patterns of permalloy-hexagons with cylinders cut-out from the center, by using a hexagonal lattice with a = 31 nm within the permalloy-layer. The form factor for the cylindrical cut-out is defined as:

$$F = 2\pi R^2 H \operatorname{sinc}\left(\frac{q_z H}{2}\right) \exp\left(\frac{iq_z H}{2}\right)\left(\frac{J_1(q_{||}R)}{q_{||}R}\right), \tag{9}$$

where, $q_{||} = \sqrt{q_x^2 + q_y^2}$, J_1 is a Bessel function of the first-kind, and radius, R = 11.2 nm, height, H = 13 nm. The magnetic phases were introduced in the permalloy-layer with a unit cell that is 12 times larger than the structure. These magnetic phases were constructed by using rectangular elements with fixed magnetization directed along its length, which were placed along the honeycomb edges with different orientations. The form factor of these rectangular elements is defined as:

$$F = LWH \operatorname{sinc}\left(\frac{q_x L}{2}\right) \operatorname{sinc}\left(\frac{q_y W}{2}\right) \operatorname{sinc}\left(\frac{q_z H}{2}\right) \exp\left(\frac{iq_z H}{2}\right), \tag{10}$$

where L, W, and H are 12.5 nm, 5 nm, and 13 nm, respectively. These magnetized-elements are placed as a part of the hexagonal lattice to incorporate long-range correlations with inter-cluster interference. The scattering matrix elements can be written as:

$$\langle \psi_i | \delta v | \psi_f \rangle = \sum_j \exp(iq_{||}R_{j||}) \int d^2r_{||} \exp(iq_{||}r_{||}) \int dz\, \boldsymbol{\phi}_i^*(z) F(r - R_{j||}; \mathbf{T}_j)\phi_f(z), \tag{11}$$

where $F(r - R_{ij}; \mathbf{T}_j)$ is the form-factor for $\mathbf{j}^{\text{th}}$ particle, such that $v_p(\mathbf{r}) = \sum_j F(r - R_{j||}; \mathbf{T}_j)$. The elastic scattering cross-section is given by: $\frac{d\sigma}{d\Omega} = \left|\langle \psi_i | \delta v | \psi_f \rangle\right|^2$. To account for the finite-size effect, we have used a 2D lattice interference function with a large isotropic 2D-Cauchy decay function with a decay length, $\lambda_{x,y}$ = 1000 nm, which is the lateral correlation length of the magnetic honeycombs such that the position-correlation is given as: $\rho_S G(\mathbf{r}) = \sum_{m,n} \delta(r - m\boldsymbol{a} - n\mathbf{b}) - \delta(\mathbf{r})$, with lattice basis (**a**, **b**) and also introduced the effects of natural-disorder of the system by applying a small Debye-Waller factor corresponding to a position-variance of $\langle x \rangle^2$ = 0.1 nm^2. The interference function can be written as:

$$S(q) = \rho_S \sum_{q_i \in \Lambda^*} \frac{2\pi\lambda_x\lambda_y}{(1 + q_x^2\lambda_x^2 + q_y^2\lambda_y^2)^{3/2}}. \tag{12}$$

For the simulation with just the structure, the magnetized elements were not introduced, and the sample contained only the coherent nuclear components. For the simulation with an external magnetic field, we allowed an external field commensurate with 0.5 T and allowed higher magnetization in the magnetized-elements corresponding to the magnetic scattering length density obtained from specular reflectivity fitting, and allowed interference with 2 other overlapping magnetic elements. It is to note that the interference between particles in different layers is not incorporated in BornAgain yet.

Electrical measurements on the sample.
Electrical measurements were performed in two-probe configuration using a synchronized combination of the Keithley current source meter 6221 and a nanovoltmeter 2182A via a trigger link. Electrical characteristic was also verified using four-probe measurement technique. The electrical contacts were made using a commercial wire bonder to 50 nm thick gold pad, deposited on the sample.

Electrical conductivity measurement of parent material, permalloy thin film of comparable thickness was also performed for comparison. As shown in Figure S6, the estimated conductivity in thin film, ~1 (Ω.cm)$^{-1}$ is in the same range as the background conductivity due to purely electrical relaxation process.

Supplemental References

Burle, J. et al. (2018). BornAgain - Software for simulating and fitting X-ray and neutron small-angle scattering at grazing incidence, version 1.15. https://www.bornagainproject.org.

Lauter, V. et al. (2019). Licorne-Py: A polarized neutron specular reflectivity fitting software. https://github.com/neutrons/Licorne-Py.

Ohl, M., Monkenbusch, M., Arend, N., Kozielewski, T., Vehres, G., Tiemann, C., Butzek, M., Soltner, H., Giesen, U., Achten, R., Lindenau, B., Budwig, A., Kleines, H., Drochner, M., Kaemmerling, P., Wagener, M., Moller, R., Iverson, E.B., Sharp, M., and Richter, D. (2012). The spin-echo spectrometer at the Spallation Neutron Source (SNS). Nucl. Instrum. Methods Phys. Res. A 696, 85-99.

Pappas, C., Ehlers, G., and Mezei, F. (2006). Neutron Scattering from Magnetic Materials, T. Chatterji, ed. (Elsevier Science), Chap. 11.